

# Stability of the Arctic Winter Atmospheric Boundary Layer over Sea Ice in CMIP6 Models

Alistair Duffey<sup>1</sup>, Robbie Mallett<sup>2</sup>, Victoria R. Dutch<sup>3,4</sup>, Julia Steckling<sup>5</sup>,  
Antoine Hermant<sup>6,7</sup>, Jonathan Day<sup>8</sup>, Felix Pithan<sup>9</sup>

<sup>1</sup>Centre for Polar Observation and Modelling, Earth Sciences, University College London, UK

<sup>2</sup>Earth Observation Group, Department of Physics and Technology, UiT The Arctic University of Norway

<sup>3</sup>School of Environmental Sciences, University of East Anglia, Norwich, Norfolk, UK

<sup>4</sup>Department of Geography and Environmental Sciences, Northumbria University, Newcastle, UK

<sup>5</sup>School of integrated climate and earth system sciences, Universität Hamburg, Hamburg, Germany

<sup>6</sup>Climate and Environmental Physics, Physics Institute, University of Bern, Switzerland

<sup>7</sup>Oeschger Centre for Climate Change Research, University of Bern, Switzerland

<sup>8</sup>European Centre for Medium-Range Weather Forecasts, Reading, United Kingdom

<sup>9</sup>Alfred Wegener Institute, Helmholtz Centre for Polar and Marine Research, Bremerhaven, Germany

## Key Points:

- A cloudy state, without strong low-level stability, is often observed over Winter Arctic sea ice but is absent in most CMIP6 models.
- CMIP6 models show a realistic representation of the dependence of low-level stability on near-surface air temperature and wind speed.
- Observations show a decreasing trend in Arctic winter low-level stability which CMIP6 models project will continue under warming.

## Abstract

The Arctic winter-time atmospheric boundary layer often features strong and persistent low-level stability which arises from longwave radiative cooling of the surface during the polar night. This stable stratification results in a positive lapse rate feedback, which is a major contributor to Arctic amplification. A second state, associated with cloudy conditions, with weaker stability and near-zero net surface longwave flux is also observed. Previous work has shown that many CMIP5 climate models fail to realistically represent the cloudy state. In this study, we assess the representation of the Arctic atmospheric boundary layer over sea ice during the winter months in global climate models contributing to the latest phase of the Coupled Model Intercomparison Project (CMIP6). We compare boundary layer process relationships seen in these models to those in surface-based and radiosonde observations collected during the recent MOSAiC (2019-2020) field campaign, alongside the earlier SHEBA (1997-1998) expedition, and from North Pole drifting stations (1955-1991). Here, we show that a majority of CMIP6 models fail to realistically represent the cloudy state over winter Arctic sea ice. Despite this, CMIP6 models have a multi-model mean low-level stability which falls within the range recorded by observational campaigns, and are mostly able to capture the observed dependence of low-level stability on near-surface air temperature and wind speed. As the Arctic warms, CMIP6 models predict a decline of winter low-level stability, with the Central Arctic's mean stability falling below zero in the multi-model mean state by the end of the century under the SSP2-4.5 emissions scenario.

## Plain Language Summary

The atmospheric boundary layer is the lowest part of the atmosphere. It is impacted by contact with the Earth's surface. In the Arctic winter, this layer of the atmosphere is often coldest nearest the surface, making it stable against convection. This feature of Arctic climate is part of the explanation for the much more rapid warming seen in the Arctic than elsewhere, known as Arctic amplification. In this study, we compare the winter Arctic boundary in climate models against that which has been observed in field campaigns. We assess the latest generation of climate models and the most recent major over-winter Arctic field campaign, MOSAiC, as well as earlier and often under-exploited observations: the SHEBA campaign and the North Pole drifting stations. We show that cloudy conditions are underrepresented in many of these models. On the other hand, models are mostly successful at representing how stability varies with temperature and wind speed. As the Arctic warms, low-level stability is expected to decrease and models project that the stable state will no longer be dominant in the Arctic winter before the end of the century under a medium emissions scenario.

## 1 Introduction

The Arctic climate system is undergoing extreme and rapid change. The region is warming nearly four times faster than the global average (Rantanen et al., 2022) and the late-summer sea ice extent has declined by 50% in 40 years (Fetterer et al., 2017, updated 2023). On land, permafrost temperature is increasing across the Arctic (Biskaborn et al., 2019) and the Greenland ice sheet is losing mass at a rate of several hundred gigatonnes per year (Otosaka et al., 2023; The IMBIE Team, 2020). Such changes are expected to continue over the coming century (e.g. Notz & Community, 2020), with global consequences including increased warming due to the albedo feedback (Pistone et al., 2014), sea level rise due to mass loss from the Greenland ice sheet (Pattyn et al., 2018), and an increased greenhouse gas burden from decomposing organic matter in thawed permafrost (Comyn-Platt et al., 2018).

The phenomenon of faster warming in the Arctic relative to lower latitudes is known as Arctic amplification. Arctic amplification is strongest in winter and largely absent in

the summer (Taylor et al., 2022). The additional warming due to Arctic amplification is globally significant; for example, it is responsible for a time difference of 5 years in the expected crossing date for the Paris agreement’s 1.5°C threshold (Duffey et al., 2023). It is driven by a combination of feedbacks including the weaker (negative) Arctic Planck feedback, increasing solar energy absorption with the decline of reflective snow and ice, and the latitudinal variation in deviation from vertically uniform warming (Goosse et al., 2018; Henry et al., 2021; Pithan & Mauritsen, 2014). This final contribution, variation in the lapse rate feedback, arises because Arctic warming is more strongly confined near the surface than warming in lower latitudes, and is one of the largest contributors to Arctic amplification in climate models (Goosse et al., 2018; Hahn et al., 2021; Lu & Cai, 2010).

During the Arctic winter, the atmosphere is often characterised by strong and long-lived low-level stability (LLS) which arises from longwave radiative cooling of the surface leading to atmospheric temperature inversions (Boeke et al., 2021; Wexler, 1936). This stable stratification of the atmospheric boundary layer causes heating to be concentrated near the surface as the Arctic climate warms, resulting in a greater temperature increase at the surface than in the upper troposphere (Manabe & Wetherald, 1975), and a positive local lapse rate feedback (Bintanja et al., 2011; Boeke et al., 2021). Sea-ice retreat and atmospheric circulation contribute to this bottom-heavy warming profile (Feldl et al., 2020). The vertical profile of Arctic warming contrasts with that seen in the tropics, where convection restores the profile close to the moist adiabat, meaning warming peaks in the upper troposphere and the lapse rate feedback is negative (Hansen et al., 1997).

Given the importance of Arctic winter-time LLS as a control on the lapse rate feedback, accurate simulation of LLS and the processes which control it are needed for reliable predictions of future Arctic climate change in global climate models. However, there are limited observations to evaluate such simulations, and large model biases persist (Solomon et al., 2023). Pithan et al. (2014) demonstrated that most CMIP5 models failed to realistically represent Arctic mixed-phase clouds and often overestimated low-level stability. Similar biases have also been documented for numerical weather prediction models (Solomon et al., 2023), with models struggling to simulate liquid water clouds at cold temperatures or to persistently represent a stable atmospheric boundary layer.

The Arctic atmospheric boundary layer in winter can generally be characterised as being in one of two states (Persson et al., 2002; Stramler et al., 2011): a clear state characterised by strong longwave surface cooling ( $\gtrsim 50 \text{ W/m}^2$ ) due to a clear lower atmosphere that is relatively transparent to outgoing radiation; and, conversely, a cloudy state in which the surface net longwave radiation is close to zero due to the presence of opaque low-level mixed phase clouds (Stramler et al., 2011). These two modes also have distinct vertical temperature structures, with stronger atmospheric inversions occurring in the clear state and weaker inversions found further aloft under the cloudy state (Stramler et al., 2011). This bimodal distribution in low-level stability is found in the CMIP5 model ensemble (Pithan & Mauritsen, 2014). However, few CMIP5 models showed a realistic representation of the cloudy state (Pithan & Mauritsen, 2014), in part due to the freezing of supercooled water droplets at excessively warm temperatures, preventing the formation of mixed phase clouds with high emissivity (Pithan & Mauritsen, 2014).

The control of stability by the wind speed and profile is another potential source of model bias which we consider. Higher near-surface wind speeds are associated with increased near-surface air temperature and a reduction in the strength of near-surface temperature inversions over Arctic sea-ice (Chechin et al., 2019; Wiel et al., 2017). Additionally, wind shear is an important control on low-level atmospheric turbulent heat fluxes in the polar night (Chechin et al., 2023).

In this study, we investigate the representation of Arctic winter low-level stability over sea ice, and the processes which control it, in the latest generation of global climate models, the CMIP6 model ensemble (Eyring et al., 2016). We compare these model representations against observations from: the Multidisciplinary drifting Observatory for the Study of Arctic Climate campaign (MOSAiC), 2019-2020, (Shupe et al., 2022); the Surface Heat Budget of the Arctic Ocean campaign (SHEBA), 1997-1998, (Uttal et al., 2002); and 21 North Polar drifting stations (NP), 1954-1990, (Kahl et al., 1999). In doing so, we build on previous work which assessed the CMIP5 ensemble against SHEBA observations (Pithan & Mauritsen, 2014), but now consider the latest generation of CMIP models and the most recent field campaign, MOSAiC, as well as exploiting the extensive NP data.

We first compare the mean-state low-level stability in CMIP6 climate models over sea-ice in winter (November to March, inclusive) to the observations. For models where the required high temporal resolution data is available, we then compare the distribution of clear and cloudy states as defined by net surface longwave radiation to the observed bimodal distribution. Next, we investigate the representation in models of various processes which control LLS, including the relationship with near-surface air temperature and the suppression of stability by surface winds. Finally, we explore future projections of Arctic winter LLS, and its contribution to Arctic amplification.

## 2 Data & Methods

### 2.1 CMIP6 Data

Our CMIP6 model ensemble is defined by the availability of data on the United Kingdom’s CEDA data archive (see Supplementary Table S1 for a list of all models used and their DOIs). At monthly resolution we analyse the output of 45 CMIP6 models, except in the case of the cloud water content and flux analysis shown in Figure 6, for which only 37 models have the required data available (see Table S1), and for the final section 4.5, which uses future projections under SSP2-4.5, for which a slightly different set of models were available (see Tables S1 and S2). For high time resolution data (6-hourly and daily), data availability is more limited and we analyse the outputs of a 20-model subset of the original 45 models. We use the first ensemble member only for each model in constructing our multi-model ensemble. Throughout, we show model output over the winter sea-ice domain. This is derived by first regridding each model’s monthly sea ice concentration onto that model’s atmospheric grid, and then defining a time-varying sea ice mask as all grid points with over 95% sea-ice concentration in a given month. Where we examine future trends, the SSP2-4.5 simulation is selected as a medium emissions scenario (Hausfather & Peters, 2020).

### 2.2 Observational Data

We compare model simulations to observational data from three sources (Figure 1). We use radiosonde and surface flux data from MOSAiC (Shupe et al., 2022) which took place from October 2019 to October 2020. Specifically, we use radiosonde data from Maturilli et al. (2021) and tower radiation data from the Atmospheric Radiation Measurement (ARM) User Facility (Reynolds & Riihimaki, 2019). Sondes were generally launched four times per day, but this frequency was increased during exceptional weather events (Peng et al., 2023). We account for this non-uniformity of time sampling in our reported mean values (see Methods). In the cold season we analyse 340 atmospheric profiles. We use radiosonde profiles and surface radiative flux data from SHEBA (Uttal et al., 2002), which took place from October 1997 to October 1998. Further information on the SHEBA radiative flux measurements is given by Persson et al. (2002). Some information on the radiosonde campaign is given in Beesley et al. (2000) and Bretherton et al. (1999), with further information available at the data source (<https://atmos.uw.edu/~roode/SHEBA.html>);

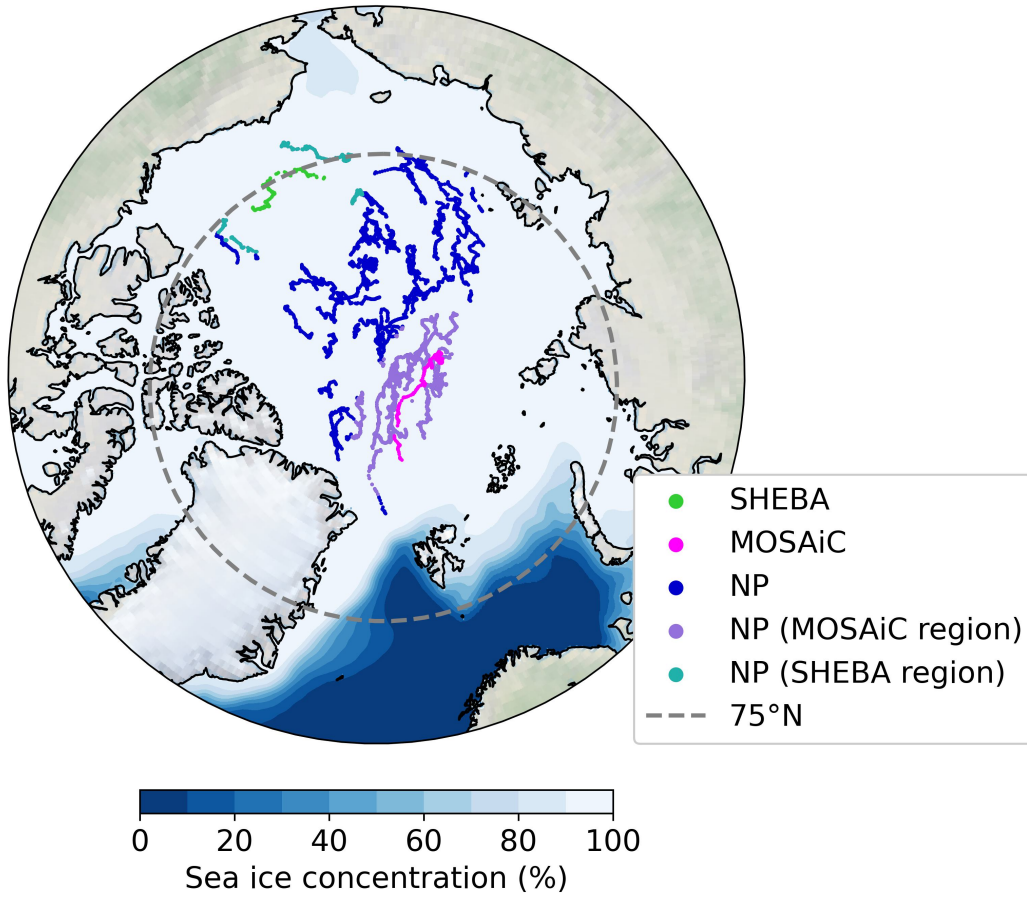


**Figure 1.** Location of winter (November-March) radiosonde observations used in this study. Arctic ocean shading shows the mean winter sea-ice concentration over the period 1950-2020 (Walsh & Stewart, 2019). NP (MOSAiC region) and NP (SHEBA region) refer, respectively, to subsets of the NP data which lie within 300 km of an observation from the MOSAiC and SHEBA campaigns.

last accessed January 2024). Radiosondes were generally launched twice daily in winter, leaving us with 276 valid winter atmospheric profiles. Finally, we also integrate radiosonde profiles from the North Pole drifting stations (NP), (Kahl et al., 1999), which operated from 1954 to 1991. While thirty-one stations existed in the time period, the archive at the US National Snow and Ice Data Centre does not contain usable observations from stations 1, 2, 18, 20, 23, 24, 25, 27, 29 & 30. As such, we use data from the remaining twenty-one stations, which leaves us with 6999 valid winter atmospheric profiles.

Combined, these three sets of observations include more than 7500 winter radiosondes, of which we can match 593 (from MOSAiC and SHEBA) to contemporaneous (within 5 minutes) surface radiative flux measurements (see Methods). These observational campaigns took place under a wide variety of ice conditions, with the icebreaker for MOSAiC surrounded by a loose assemblage of second-year ice (Krumpal et al., 2021) and that of SHEBA surrounded by multi-year ice (Perovich et al., 2003). While sparse in both time and space, our collection of observations gives some coverage across much of the Arctic ocean domain, and samples across a time period of nearly 70 years. The difference between NP stations also gives valuable insight into the size of interannual variability.

### 2.3 Methods

Our analysis focuses on the representation of atmospheric boundary layer processes, assessed via the relationships between model variables. To do this we construct the set of all extended-winter (November-march), hereafter ‘winter’, sea-ice grid points and time points for 6-hourly or daily data under the final decade of the historical simulation (Eyring et al., 2016), over which we assess variable distributions for each model. Each observation from a field campaign is not strictly equivalent to a random draw from these model distributions; observations have different seasonal and regional sampling, and additionally, observations are instantaneous and at one point in space, whereas model data is the time-step and grid-cell mean.

Where the mean state is compared between models and observations (e.g. Figure 2), we account for the imperfect temporal sampling in observations in two steps. First, we group the individual sonde observations by date, such that the mean is not biased towards days with additional sonde launches. This is most impactful for MOSAiC, where additional sondes were launched on days of exceptional weather (Peng et al., 2023). Second, we account for inconstant seasonal sampling by first grouping the observational data by month and then taking the full winter mean. Where a ‘mean’ value over time is quoted below for observations, this always refers to a temporally representative value estimated in this manner, as opposed to a simple mean of all observations within the winter period in the data set.

We consider whether each model shows a bimodal distribution in surface net long-wave radiation, as a metric for showing distinct clear and cloudy states (Pithan & Mauritsen, 2014; Stramler et al., 2011). As a statistical test for this bimodality, we use Hartigan’s ‘Dip’ test (J. A. Hartigan & Hartigan, 1985; P. M. Hartigan, 1985), which tests whether a unimodal or multimodal distribution is a better fit to a distribution. We refer to models as ‘bimodal’ where this test rejects the null hypothesis of unimodality at the 95% significance level.

Having characterised the bulk LLS following the method above, we assess its suppression by wind. We do this by retrieving the surface wind speed of individual sondes in our three observational data sets, then pairing the speeds with the LLS observed by the same sondes. We produced 189, 341 & 7753 of these paired data points from the MOSAiC, SHEBA and North Pole stations respectively. Surface wind speeds from the North Pole sondes were recorded only to the nearest  $\text{ms}^{-1}$ . We then compare both the strength



and gradient of our observed relationships between LLS and surface wind speed to those in CMIP6 models.

Following Medeiros et al. (2011) and Pithan et al. (2014), we assess the bulk low-level stability (LLS), defined as the difference between the 850hPa level temperature and the near-surface (2m) air temperature, as a proxy for the temperature inversion. We define the LLS as positive where the temperature is warmer aloft. This proxy is useful given the low and variable vertical resolution of CMIP6 models, which complicates direct comparison to radiosonde profiles.

### 3 Results

#### 3.1 Mean-state Low-Level Stability

We begin by assessing the LLS over Arctic sea-ice during the winter months across the CMIP6 model ensemble and our three observational datasets (Figure 2). The mean LLS values in MOSAiC, SHEBA and NP are  $5.0 \pm 0.3$ ,  $8.3 \pm 0.4$  and  $9.5 \pm 0.1$  °C, respectively, where the errors quoted are the standard error of the mean. We account for uneven temporal sampling in our calculation of these values (see Methods). The three sets of observations were collected at different locations which will influence their LLS. For example, weaker mean stability is expected in the Atlantic Sector (MOSAiC) compared to the Beaufort Gyre (SHEBA) (Liu et al., 2006). To estimate the significance of this different regional sampling, we subset the NP data to keep only those measurements within 300 km of any observations from first, MOSAiC and second, SHEBA. The locations of these subsets of the NP data are shown in Figure 1. Calculating the mean LLS for these regional subsets of the NP data shows that location is not the primary driver of variation in observed LLS. NP stations within 300 km of the MOSAiC campaign have a mean LLS of  $9.3 \pm 0.1$  °C, which is lower than the full NP mean, but by only 0.2 °C, as compared to the 4.5 °C difference between MOSAiC and NP. For NP stations within 300 km of the SHEBA campaign, mean LLS is  $9.3 \pm 0.3$  °C which, similarly, is closer to the full NP mean than the SHEBA mean.

Even accounting for location, we would not expect the mean LLS to be identical across these observational data. Other contributors to the difference include interannual variability — SHEBA and MOSAiC each represent only a single winter — and any long-term temporal trend over the period 1950 - 2020. The standard deviation of the mean values of LLS for each NP station is 0.94 °C, which gives a rough estimate of the size of interannual variability, and the minimum mean for a station is 7.6 °C. The three sets of observations show a chronological reduction in LLS between the data sources, with the earliest (NP) having the strongest LLS. Since the MOSAiC mean LLS is well outside the range of the NP stations, it seems plausible that decrease in LLS across the three datasets is representative of a wider Arctic trend. Such a negative trend would be expected given the clear negative trend under warming seen in the CMIP6 ensemble (see Section 3.5).

In the multi-model mean, the winter boundary layer over sea ice is characterised by mean low-level stability of 6.6°C, as calculated over the final two decades of the historical simulation (1995 - 2015). This mean value is within the range of mean states (5 - 10°C) seen across the three observational datasets. Two models (CESM2-WACCM-FV2 and E3SM-1-0) out of 45 show negative winter mean LLS over sea ice. A large majority of models show a strong differentiation between open ocean and sea-ice regions, without low-level stability over the open ocean in the monthly mean state (Figure S1); only 3 models out of 45 (GISS-E2-1-H, GISS-E2-2-H, and NorCPM1) have positive winter mean-state LLS over the open ocean North of 65°N.

We now investigate the representation of process relationships which control the boundary layer stability in CMIP6 models. We compare the CMIP6 models against ob-

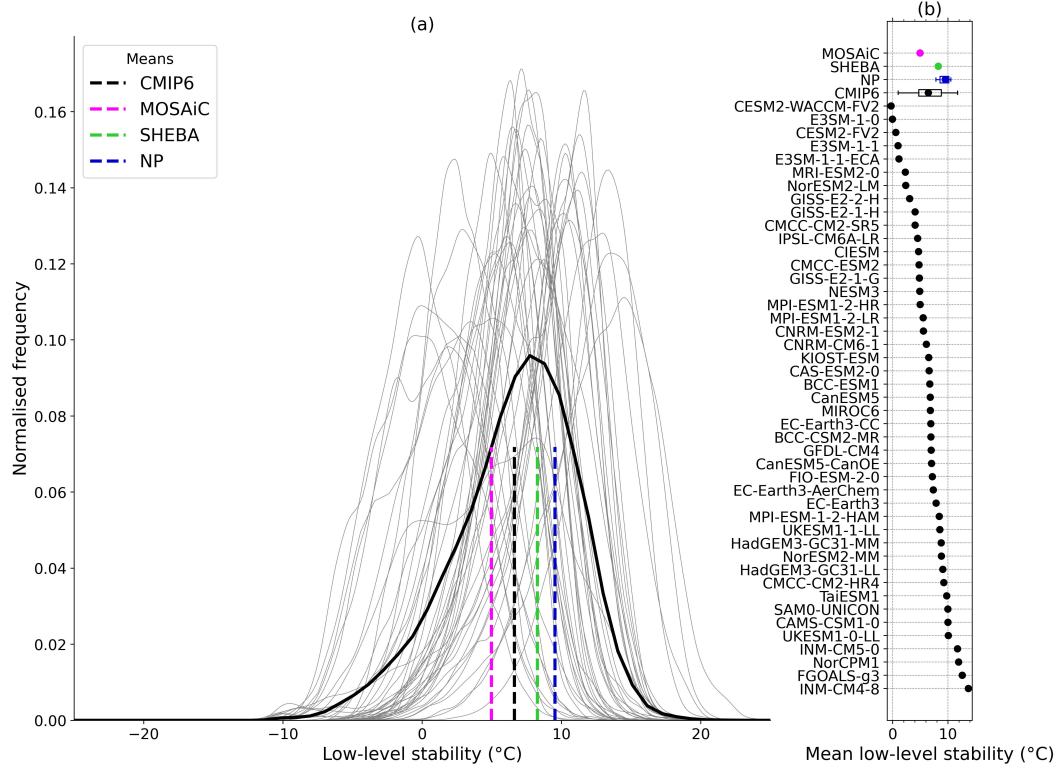


**Figure 2.** (a) Mean low-level stability over Arctic sea ice in the winter months (November–March) in CMIP6 models and observations. (b) Distribution of winter low-level stability over Arctic sea-ice (>95% concentration) in CMIP6 models (gray) and field campaigns (colors). Low-level stability is defined as the difference between temperature at 850hPa and the 2m air temperature. The bold black line is the multi-model distribution. For all models, the distribution shown is over all grid points in time and space where sea-ice concentration is greater than 95%, over the period 1995–2015, and the region North of 65°N. Vertical dashed lines denote mean values.



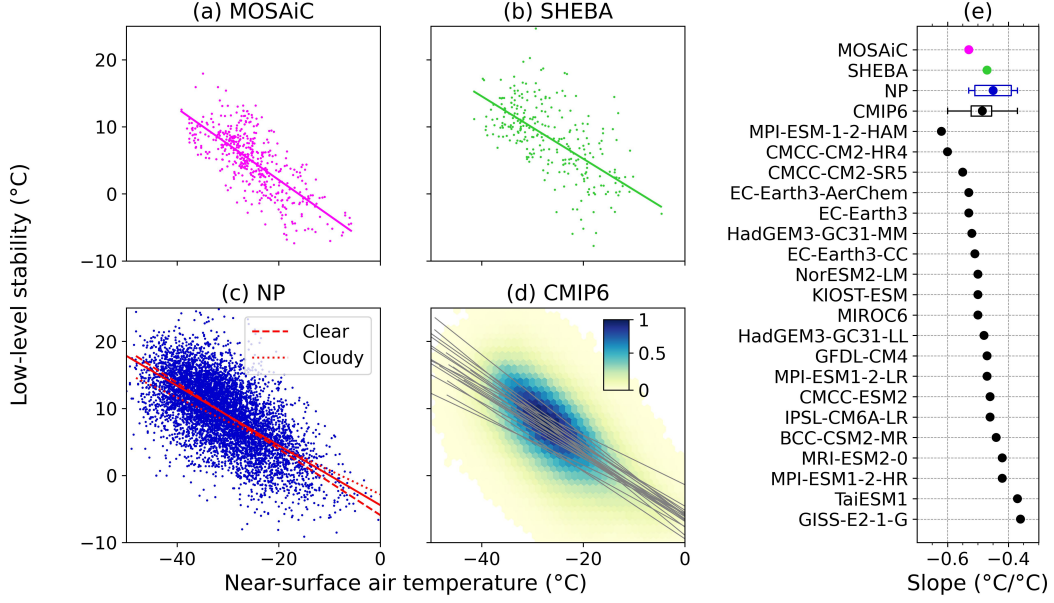


**Figure 3.** Relationship between winter near-surface air temperature and low-level stability, in observations (a-c) and CMIP6 models over sea ice (d). Individual radiosondes are shown for observations, and relative density of time and grid point instances over sea ice as a histogram with arbitrary density units for CMIP6 models. Data for all models is 6-hourly, except for NorESM2-LM, IPSL-CM6A-LR, EC-Earth3-CC, and TaiESM1, which use daily mean outputs. Solid lines are linear regressions, with one grey line for each CMIP6 model assessed. In the case of NP, we also show regressions on the subsets of observations under ‘clear’ and ‘cloudy’ conditions defined as less than, and greater than 50% cloud cover by visual assessment, respectively. Plot (e) shows the slopes of the regressions given in plots a-d.

servations in terms of their variation in LLS with, first, near-surface air temperature, second, the net surface longwave flux, and third, surface wind strength.

### 3.2 Near-surface air temperature as a control on low-level stability

Observations display a linear relationship between LLS and the near-surface air temperature (Figure 3). Such a relationship has been reported previously by Liu et al. (2006), and is consistent between all three observational datasets. LLS decreases by approximately  $0.5^{\circ}\text{C}$  per  $1^{\circ}\text{C}$  increase in near-surface air temperature, i.e., the temperature at 850 hPa increases only approximately  $0.5^{\circ}\text{C}$  per  $1^{\circ}\text{C}$  increase at the surface. This relationship is also seen consistently across the ensemble of high-time resolution CMIP6 models. The multi-model mean change in LLS with near-surface air temperature is  $-0.47^{\circ}\text{C}/^{\circ}\text{C}$ , and the standard deviation across models is  $0.06^{\circ}\text{C}/^{\circ}\text{C}$ . CMIP6 models, therefore, are successful in capturing the observed coupling on short timescales between temperature at the surface and LLS over sea ice during winter.

### 3.3 Clear and cloudy states

As described in the introduction, observations support a binary classification of the Arctic winter boundary layer into two states; a clear-sky state with strong longwave radiative cooling of the surface and strong LLS, and, a cloudy state with near zero surface net longwave flux and weak or negative LLS (Stramler et al., 2011). By plotting bivari-

ate histograms of LLS and net surface longwave (Figure 4), we can see a distinct clear/cloudy bimodality in the MOSAiC and SHEBA data. Defining any observation with surface net longwave more negative than  $-25 \text{ W/m}^2$  (the dotted lines in Figure 4) as being in the clear state, the clear state accounts for approximately 60% of observations (MOSAiC 65%, SHEBA 59%, NP 63%). Surface longwave fluxes time-matched to radiosonde observations were not available for the NP dataset, so we split the LLS observations into two states (Figure 4c), with the clear state defined as less than 50% cloud cover by visual assessment. The proportion of NP observations in the clear state by visual assessment is not strongly sensitive to the choice of threshold because the large majority (79%) of visual observations are either under 10% cloud cover, or over 80% cloud cover. Using alternative clear-sky thresholds of less than 30% or less than 70% would result in the clear state accounting for 57% and 66% of observations, respectively.

Across the CMIP6 models assessed, we find inconsistency in the representation of these two states (clear & cloudy). A visual assessment shows some models, such as MRI-ESM2-0, with a second centre of density at close to zero net LW flux which we attribute to the cloudy state, while other models, such as TaiESM1, have a single mode at approximately  $-50 \text{ W/m}^2$  net LW, which we identify as having only a clear state. Using a statistical test for multimodality (the Dip test, see Methods) on the distribution of 6-hourly net surface LW in each model, we categorise the 20 models in Figure 4 into those which show and those which do not show the two states. The one-dimensional histogram of net surface LW for each model on which this distinction is based is shown in Supplementary Figure S3. Seven out of 20 models show a bimodal distribution, with both clear and cloudy atmospheric states (denoted with a \* in Figure 4). The ordering of models by their mean column cloud condensed water content (i.e. the ice water path plus the liquid water path) also supports our association of the lack of second mode in LLS with a lack of a cloudy state; those models which lack the cloudy state as assessed based on LW flux and low-level stability also show the least atmospheric cloud water content. The spread amongst models in their cloud condensed water content is very large, ranging between 1 and  $65 \text{ g/m}^2$ . The equivalent mean value for MOSAiC is approximately  $80 \text{ g/m}^2$ , as calculated from the dataset of Saavedra Garfias et al. (2023) produced from MOSAiC microwave and radar observations. As such, the higher end of the model range appears more likely to be realistic, although we would expect the MOSAiC mean-state to be higher than the regional average shown for the models because moist intrusions are more common in the Atlantic sector of the Arctic (Woods & Caballero, 2016).

For the seven models showing a bimodal LLS distribution, we again use a  $-25 \text{ W/m}^2$  cutoff value to assign data points into one of the two states, as shown in Supplementary Table S3. Four models (BCC-CSM2-MR, MPI-ESM1-2-LR, MPI-ESM1-2-HR, and NorESM2-LM) show an overrepresentation of the cloudy state relative to observations. Within the MPI-ESM1 family of models, it appears that model physics rather than resolution is the greater control on realistically representing these states. MPI-ESM1-2-HAM, which has interactive aerosols as well as altered mixed-phase microphysics, has improved realism in the distribution of clear and cloudy states relative to MPI-ESM1-2-LR and MPI-ESM1-2-HR. Both have a minority of data points in the clear state, while MPI-ESM1-2-HAM has 60% of points in the clear state, broadly in line with the observations. Alongside the overrepresentation of the cloudy state, MPI-ESM1-2-LR and MPI-ESM1-2-HR also have mean LLS of  $5.7$  and  $5.0 \text{ }^\circ\text{C}$ , respectively, at the low end of the CMIP6 range, while MPI-ESM1-2-HAM has stronger stability of  $7.7 \text{ }^\circ\text{C}$ .

Comparing the distributions shown in Figure 4 with the mean state LLS by model in Figure 2, we can see that the inter-model spread in LLS is determined, not only by the relative frequency of the two modes, but also by the central LLS value within each mode. For example, while MRI-ESM2-0 has a realistic 63% of points with under  $-25 \text{ W/m}^2$  net LW (the cloudy state), it has the lowest mean LLS of the models in Figure 4 because both modes are found at too negative values of LLS.

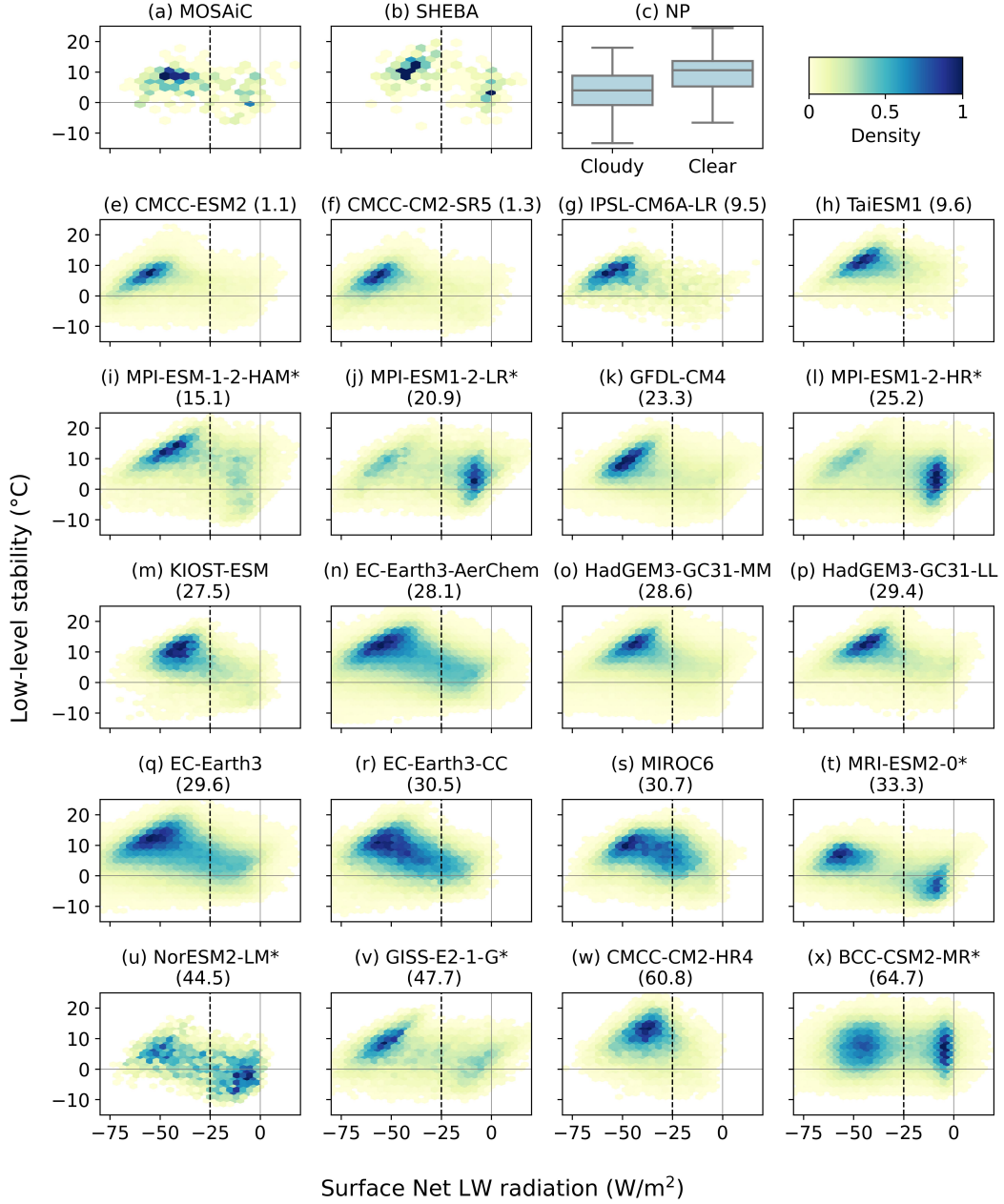


**Figure 4.** Bivariate histograms of net longwave radiation at the surface (positive downward) against low-level stability over sea ice, during the winter months (November-March). Histogram units are an arbitrary density, as the total count of points varies between subplots. Surface radiative flux was not available for the North Pole drifting stations (NP) so NP data is partitioned based on visual assessment of cloud coverage, with coverage of  $>50\%$  denoted ‘Cloudy’. Data for all models is 6-hourly, except for NorESM2-LM, IPSL-CM6A-LR, EC-Earth3-CC, and TaiESM1, which use daily mean outputs. The values in brackets in each title are the mean-state atmosphere mass content of cloud condensed water ( $\text{grams}/\text{m}^2$ ) for each model over the same region and time period; the models are shown in ascending order in this quantity. Starred models are not unimodal in net longwave radiation, according to a Dip test at 95% significance (see Methods and Supplementary Figure S3).

### 3.4 Other controls on low-level stability

We now consider surface wind speed as a control on LLS. The observed relationship between near-surface inversions and wind speed is non-linear, with several studies finding transition wind speeds, above which the surface inversion strength sharply decreases to near-zero (Wiel et al., 2017). At the bulk scale of our analysis, such a transition is not apparent (Figure 5, a-c), and we here use a linear regression analysis as a first-order approximation to the non-linear underlying behaviour. In Figure 5 we show this relationship for our three observational data sets, and for 12 CMIP6 models for which wind variables were available at daily (or higher) resolution. The three sets of observations show clear and highly statistically significant reductions in LLS with faster surface wind speed of  $-0.55$ ,  $-0.67$  and  $-0.63^\circ\text{C}$  per  $\text{ms}^{-1}$  in MOSAiC, SHEBA, and NP, respectively, and  $R^2$  values of approximately 0.1 in each case. For NP, this reduction in LLS with increasing wind speed holds both across all stations, and within every individual station.

The CMIP6 models show a diverse set of wind speed-LLS relationships. Several models (e.g. IPSL-CM6A-LR) recreate the observed wind suppression closely, with a slope of approximately  $-0.6^\circ\text{C}/\text{ms}^{-1}$  and wind speed accounting for approximately 10% of the variance in LLS. However, one model (BCC-CSM2-MR) shows a strong and significant increase in LLS with wind speed, and another (MRI-ESM2-0) shows almost no relationship, with  $R^2$  less than 0.01. Part of this variation is likely driven by differences in the mean-state wind shear amongst the models. We would expect an increase in wind-driven atmospheric turbulent heat fluxes with stronger wind shear (Chechin et al., 2023), and as a result, a stronger suppression of low-level stability. This relationship is seen (not shown) in the NP station data, for which there is a positive correlation (significant at 90% confidence) between the mean-state wind shear at a particular station, and the reduction in stability with wind speed recorded at that station. The variation in wind shear between NP stations includes contributions from synoptic variability and local sea ice conditions, whereas variability in wind-shear between models, for which the mean state is over the entire winter Arctic sea-ice domain over 20 model years in each case, is likely predominantly due to model uncertainty.

Possible contributors to the lack of cloudy state seen in some climate models include: synoptic-scale meteorology (e.g. not enough moisture flux into the Arctic), column physics/surface-atmosphere coupling (e.g. bias in vertical turbulent heat fluxes at surface), and cloud microphysics (e.g. early freezing of supercooled water droplets (Pithan et al., 2014)). The first of these, synoptic-scale meteorology is out of the scope of this study to assess, but we now make a limited assessment of the potential contribution from the second and third options across the CMIP6 ensemble. Figure 6a shows the relationship between cloud ice fraction and mean-state low-level stability. The positive relationship here suggests that the freezing of supercooled liquid droplets at excessively warm temperatures and resulting inability to maintain high emissivity mixed-phase clouds, which contributed to the lack of a cloudy state in CMIP5 models (Pithan et al., 2014), may also persist in CMIP6 models which lack a cloudy state. However, since we establish only a correlation across the model ensemble here, the reverse relationship is also possible; it may be that models with strong LLS and thus a cold boundary layer see greater condensate freezing. Finally, across the CMIP6 ensemble, there is a strong negative relationship between mean-state surface upward sensible heat flux and low-level stability over sea ice during the winter months (Figure 6b). This relationship can be explained in terms of the stronger downward fluxes expected given a steeper temperature gradient in the atmospheric column.

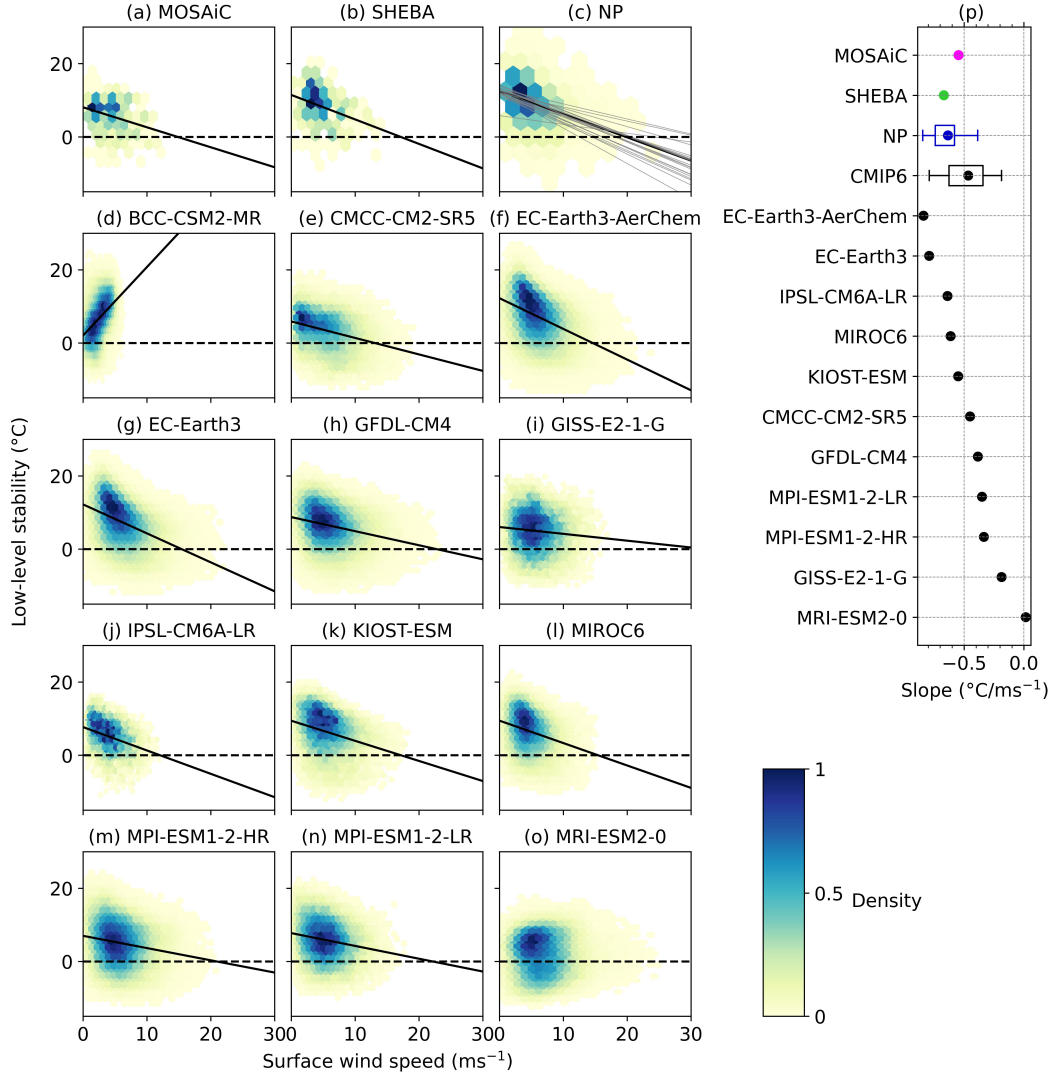


**Figure 5.** Relationship between low-level stability and surface wind speed during the winter months (November-March) in each of the three sets of observations (a-c), and the 12 models for which wind data was available (d-o). Solid lines are linear regressions and colors are bivariate histograms with arbitrary density units (as the total count of points varies between subplots). For NP (subplot c), gray solid lines show the linear regression as calculated for each individual drifting station. All regressions plotted have a p-value less than 0.001. Plot (p) shows the values of the slopes of each linear regression. BCC-CSM2-MR, which has a strongly positive slope, is excluded from subplot (p) and from the CMIP6 distribution shown as a box. For NP, the distribution of slopes across individual stations is shown as a box.

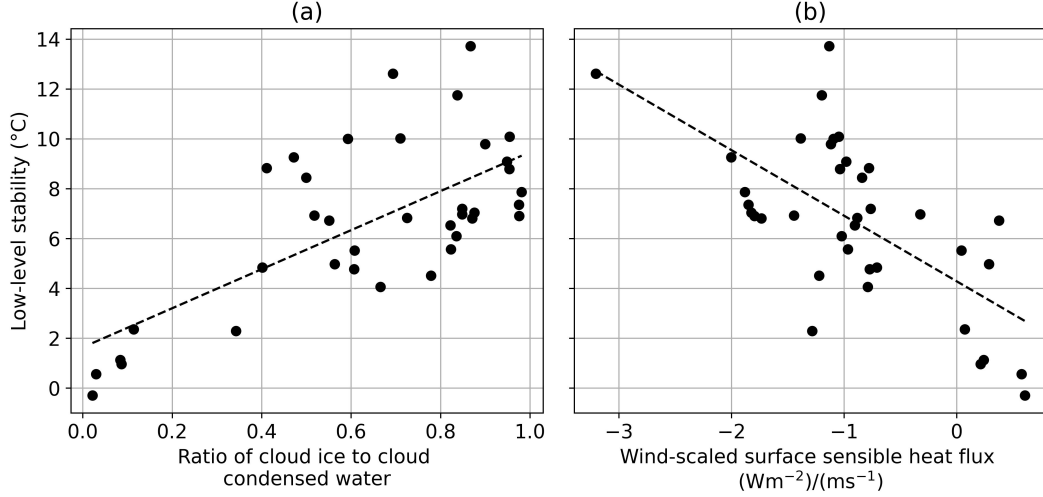


**Figure 6.** (a) Ratio of atmospheric column cloud ice to atmospheric column condensed water across the multi-model ensemble in the mean state. (b) Relationship between low-level stability and surface sensible heat flux scaled by the surface wind speed. In both panels, each point represents the mean of all monthly instances of LLS and each variable for the 1st ensemble member over the winter months (November-March) over the sea ice region in a given model over the final two decades of the historical simulation (1995-2015).

### 3.5 Projected decline in low-level stability under warming

We have shown (Figure 3) that LLS and near-surface air temperature are negatively correlated in both CMIP6 models and observations on short timescales of hours to days, such that temperatures aloft at 850hPa increase by  $\sim 0.5^{\circ}C$  for each  $1^{\circ}C$  increase at the surface. In Supplementary Figure S4 we demonstrate that this linear relationship also applies on climatic timescales in each individual CMIP6 model. Over the 250 years of the historical and SSP2-4.5 runs, we find a significant ( $p > 99\%$ ) negative linear relationship between winter near-surface air temperature over Arctic sea ice and LLS in all 40 models assessed. This decrease in LLS with surface warming of  $-0.6 \pm 0.1^{\circ}C/^{\circ}C$  is equivalent to an increase in temperature aloft (850 hPa) of  $+0.4^{\circ}C$  per  $^{\circ}C$  surface warming. As a consequence of this, Figure 7 demonstrates how with amplified Arctic wintertime warming over the 21st century under the SSP2-4.5 emissions scenario, we see a decrease in wintertime LLS. Northward of  $75^{\circ}N$ , the multi-model mean LLS declines from  $6.9^{\circ}C$  in the pre-industrial period to become negative before the end of the 21st century, with the 10-year rolling mean crossing the zero line in 2083. The rate of decline in LLS across the observations, of  $-0.85^{\circ}C$  per decade, is nearly twice as large as the  $-0.45^{\circ}C$  per decade trend seen in the CMIP6 multi-model mean over the same period.

## 4 Summary

In this paper we have assessed the representation of Arctic atmospheric boundary layer processes over sea ice during winter in CMIP6 climate models. Radiosondes from our three datasets find mean wintertime LLS over sea ice of between  $5 - 10^{\circ}C$ , with the large range likely arising at least in part due to a decreasing trend in LLS over the 70 year time-span between the campaigns. The CMIP6 multi-model mean LLS over winter sea ice sits within this range at  $7.0^{\circ}C$ . However, individual models show a large range of mean states, with several models having negative LLS and thus failing to show a typ-



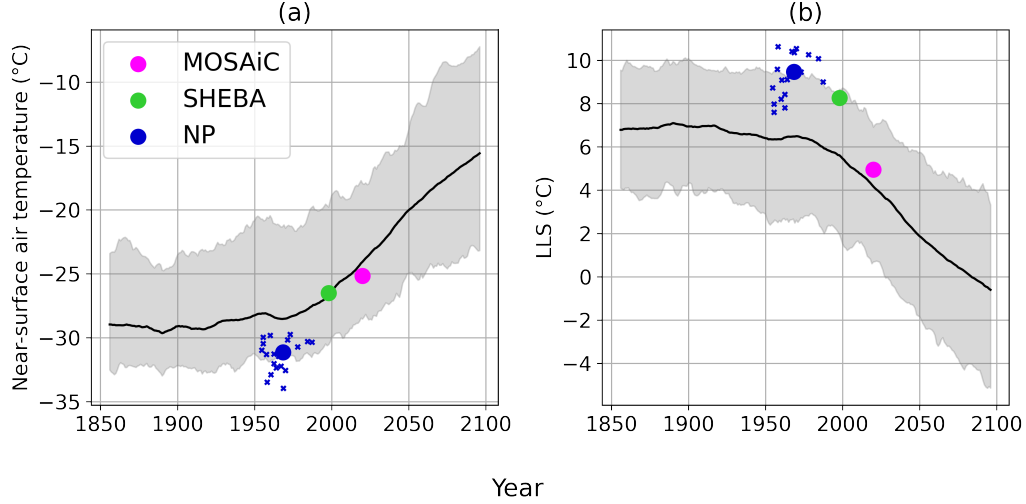


**Figure 7.** Time series of the CMIP6 multi-model ensemble projections for (a) High Arctic (>75°N) winter near-surface air temperature change, and (b) High Arctic (>75°N) low-level stability. The black line is the multi-model mean of 10-year centred rolling means, and the shaded region is the 10 to 90th percentile range. The coloured dots show the mean values in each observational campaign, with smaller dots for individual NP stations.

ically stable boundary layer. Models with high LLS often lack a cloudy state. This lack of a cloudy state, characterised by near-zero net surface longwave flux and weaker, elevated, inversions, reported by Pithan et al. (2014) for CMIP5, still applies for a majority of models in this newer generation. Despite this, we show that all models assessed reproduce the observed negative linear relationship between near-surface air temperature and LLS in the Arctic winter over sea-ice, with approximately a 0.5°C decrease in LLS per °C warming at the surface. Suppression of stability with greater surface winds is also found in the CMIP6 models, albeit less consistently. Both the NP drifting stations and the CMIP6 models show greater wind suppression with increased wind shear.

In addition to the negative correlation between near-surface air temperature and stability which operates on short timescales of hours to days, we also find that a negative linear relationship between near-surface air temperatures and LLS holds over long-term climatic timescales in the CMIP6 models due to ‘bottom-heavy’ Arctic warming. As the Arctic warms, the multi-model CMIP6 mean shows winter LLS decreasing to zero in the central Arctic in the CMIP6 mean before the end of the century under the medium emissions scenario SSP2-4.5. Future work might consider the implications of this declining stability for the model representation of the Arctic boundary layer. Here, we simply note that this transition away from a typically stably stratified wintertime boundary layer marks yet another dramatic change in Arctic climate projected under amplified Arctic warming in the coming decades.

## 5 Open Research

All data used in this work are publically available. The CMIP6 data can be accessed from the Earth System Grid Federation CMIP6 archive (<https://esgf-index1.ceda.ac.uk/search/cmip6-ceda/>). The North Polar drifting stations observations are available to download online from the National Snow and Ice Data Centre, (Colony & Thorndike, 1984). MOSAiC data is available from Pangea (Maturilli et al., 2021) and MOSAiC tower radiation data

can be downloaded from <https://www.arm.gov> at the DOI <https://doi.org/10.5439/1608608>.  
 SHEBA data can be downloaded at <https://atmos.uw.edu/roode/SHEBA.html>. Code  
 to perform all analysis and plotting is available at [https://github.com/alistairduffy/ABL\\_CMIP6](https://github.com/alistairduffy/ABL_CMIP6).

## Acknowledgments

This study was initiated at the CLIVAR Arctic Processes in CMIP6 Bootcamp, October 2022. We are grateful to organizer Ruth Mottram and all lecturers and mentors for their work. We are also grateful to all those involved in the MOSAiC, SHEBA and North Pole Drifting Station field campaigns for collecting and making publicly available the data used in this analysis. AD acknowledges funding from the London Natural Environment Research Council (NERC) Doctoral Training Partnership (DTP) Grant NE/S007229/1. RM acknowledges funding from the Canada 150 Research Chairs Program via Julianne Stroeve, which supported some of this work at the University of Manitoba. FP acknowledges funding from the European Union's Horizon 2020 research and innovation programme under grant agreement No. 101003826 via project CRiceS (Climate Relevant interactions and feedbacks: the key role of sea ice and Snow in the polar and global climate system). VRD was supported by a Research Development Fund (RDF) studentship from Northumbria University and the Northern Water Futures project.

## References

- Beesley, J. A., Bretherton, C. S., Jakob, C., Andreas, E. L., Intrieri, J. M., & Uttal, T. A. (2000). A comparison of cloud and boundary layer variables in the ECMWF forecast model with observations at Surface Heat Budget of the Arctic Ocean (SHEBA) ice camp. *Journal of Geophysical Research: Atmospheres*, 105(D10), 12337–12349. Retrieved 2024-02-06, from <https://onlinelibrary.wiley.com/doi/abs/10.1029/2000JD900079> (eprint: <https://onlinelibrary.wiley.com/doi/pdf/10.1029/2000JD900079>) doi: 10.1029/2000JD900079
- Bintanja, R., Graverson, R. G., & Hazeleger, W. (2011, November). Arctic winter warming amplified by the thermal inversion and consequent low infrared cooling to space. *Nature Geoscience*, 4(11), 758–761. Retrieved 2023-01-06, from <https://www.nature.com/articles/ngeo1285> (Number: 11 Publisher: Nature Publishing Group) doi: 10.1038/ngeo1285
- Biskaborn, B. K., Smith, S. L., Noetzli, J., Matthes, H., Vieira, G., Streletskiy, D. A., ... Lantuit, H. (2019, January). Permafrost is warming at a global scale. *Nature Communications*, 10(1), 264. Retrieved 2023-01-23, from <https://www.nature.com/articles/s41467-018-08240-4> (Number: 1 Publisher: Nature Publishing Group) doi: 10.1038/s41467-018-08240-4
- Boeke, R. C., Taylor, P. C., & Sejas, S. A. (2021). On the Nature of the Arctic's Positive Lapse-Rate Feedback. *Geophysical Research Letters*, 48(1), e2020GL091109. Retrieved 2023-08-23, from <https://onlinelibrary.wiley.com/doi/abs/10.1029/2020GL091109> (eprint: <https://onlinelibrary.wiley.com/doi/pdf/10.1029/2020GL091109>) doi: 10.1029/2020GL091109
- Bretherton, C. S., de Roode, S. R., Jakob, C., Andreas, E. L., Intrieri, J., & Persson, P. O. G. (1999). A comparison of the ECMWF forecast model with observations over the annual cycle at SHEBA. *Journal of Geophysical Research (Fire Arctic Clouds Experiment Special Issue)*. Retrieved from <https://dspace.library.uu.nl/bitstream/handle/1874/2608/sheba2.pdf?sequence=1&isAllowed=y>
- Chechin, D. G., Lüpkes, C., Hartmann, J., Ehrlich, A., & Wendisch, M. (2023, April). Turbulent structure of the Arctic boundary layer in early summer driven by stability, wind shear and cloud-top radiative cooling: ACLOUD air-

- borne observations. *Atmospheric Chemistry and Physics*, 23(8), 4685–4707. Retrieved 2023-10-24, from <https://acp.copernicus.org/articles/23/4685/2023/> (Publisher: Copernicus GmbH) doi: 10.5194/acp-23-4685-2023
- Chechin, D. G., Makhotina, I. A., Lüpkes, C., & Makshtas, A. P. (2019, August). Effect of Wind Speed and Leads on Clear-Sky Cooling over Arctic Sea Ice during Polar Night. *Journal of the Atmospheric Sciences*, 76(8), 2481–2503. Retrieved 2023-10-24, from <https://journals.ametsoc.org/view/journals/atsc/76/8/jas-d-18-0277.1.xml> (Publisher: American Meteorological Society Section: Journal of the Atmospheric Sciences) doi: 10.1175/JAS-D-18-0277.1
- Colony, R., & Thorndike, A. S. (1984). *Arctic Ocean Drift Tracks from Ships, Buoys, and Manned Research Stations, 1872-1973, Version 1*. National Snow and Ice Data Center. Retrieved from <https://nsidc.org/data/G01358/versions/1> doi: 10.7265/N5D798B1
- Comyn-Platt, E., Hayman, G., Huntingford, C., Chadburn, S. E., Burke, E. J., Harper, A. B., ... Sitch, S. (2018, August). Carbon budgets for 1.5 and 2 °C targets lowered by natural wetland and permafrost feedbacks. *Nature Geoscience*, 11(8), 568–573. Retrieved 2023-03-16, from <https://www.nature.com/articles/s41561-018-0174-9> (Number: 8 Publisher: Nature Publishing Group) doi: 10.1038/s41561-018-0174-9
- Duffey, A., Mallett, R., Irvine, P. J., Tsamados, M., & Stroeve, J. (2023, May). ESD Ideas: Arctic Amplification’s Contribution to Breaches of the Paris Agreement. *EGUsphere*, 1–7. Retrieved 2023-08-25, from <https://egusphere.copernicus.org/preprints/2023/egusphere-2023-810/> (Publisher: Copernicus GmbH) doi: 10.5194/egusphere-2023-810
- Eyring, V., Bony, S., Meehl, G. A., Senior, C. A., Stevens, B., Stouffer, R. J., & Taylor, K. E. (2016, May). Overview of the Coupled Model Intercomparison Project Phase 6 (CMIP6) experimental design and organization. *Geoscientific Model Development*, 9(5), 1937–1958. Retrieved 2024-01-04, from <https://gmd.copernicus.org/articles/9/1937/2016/gmd-9-1937-2016.html> (Publisher: Copernicus GmbH) doi: 10.5194/gmd-9-1937-2016
- Feldl, N., Po-Chedley, S., Singh, H. K. A., Hay, S., & Kushner, P. J. (2020, October). Sea ice and atmospheric circulation shape the high-latitude lapse rate feedback. *npj Climate and Atmospheric Science*, 3(1), 1–9. Retrieved 2024-02-05, from <https://www.nature.com/articles/s41612-020-00146-7> (Number: 1 Publisher: Nature Publishing Group) doi: 10.1038/s41612-020-00146-7
- Fetterer, F., Knowles, K., Meier, W. N., Savoie, M., & Windnagel, A. K. (2017). *Sea Ice Index, Version 3*. Boulder, Colorado USA. NSIDC: National Snow and Ice Data Center. Retrieved from <https://doi.org/10.7265/N5K072F8>
- Goosse, H., Kay, J. E., Armour, K. C., Bodas-Salcedo, A., Chepfer, H., Docquier, D., ... Vancoppenolle, M. (2018, May). Quantifying climate feedbacks in polar regions. *Nature Communications*, 9(1), 1919. Retrieved 2022-02-14, from <https://www.nature.com/articles/s41467-018-04173-0> (Number: 1 Publisher: Nature Publishing Group) doi: 10.1038/s41467-018-04173-0
- Hahn, L. C., Armour, K. C., Zelinka, M. D., Bitz, C. M., & Donohoe, A. (2021). Contributions to Polar Amplification in CMIP5 and CMIP6 Models. *Frontiers in Earth Science*, 9. Retrieved 2022-02-14, from <https://www.frontiersin.org/article/10.3389/feart.2021.710036>
- Hansen, J., Sato, M., & Ruedy, R. (1997). Radiative forcing and climate response. *Journal of Geophysical Research: Atmospheres*, 102(D6), 6831–6864. Retrieved 2023-09-25, from <https://onlinelibrary.wiley.com/doi/abs/10.1029/96JD03436> (eprint: <https://onlinelibrary.wiley.com/doi/pdf/10.1029/96JD03436>) doi: 10.1029/96JD03436
- Hartigan, J. A., & Hartigan, P. M. (1985, March). The Dip Test of Unimodality.

- 549 *The Annals of Statistics*, 13(1), 70–84. Retrieved 2023-11-08, from [https://](https://projecteuclid.org/journals/annals-of-statistics/volume-13/issue-1/The-Dip-Test-of-Unimodality/10.1214/aos/1176346577.full)  
 550 [projecteuclid.org/journals/annals-of-statistics/volume-13/issue-1/](https://projecteuclid.org/journals/annals-of-statistics/volume-13/issue-1/The-Dip-Test-of-Unimodality/10.1214/aos/1176346577.full)  
 551 [The-Dip-Test-of-Unimodality/10.1214/aos/1176346577.full](https://projecteuclid.org/journals/annals-of-statistics/volume-13/issue-1/The-Dip-Test-of-Unimodality/10.1214/aos/1176346577.full) (Publisher:  
 552 Institute of Mathematical Statistics) doi: 10.1214/aos/1176346577
- 553 Hartigan, P. M. (1985). Computation of the Dip Statistic to Test for Uni-  
 554 modality. *Journal of the Royal Statistical Society: Series C (Applied*  
 555 *Statistics)*, 34(3), 320–325. Retrieved 2023-11-08, from [https://](https://onlinelibrary.wiley.com/doi/abs/10.2307/2347485)  
 556 [onlinelibrary.wiley.com/doi/abs/10.2307/2347485](https://onlinelibrary.wiley.com/doi/abs/10.2307/2347485) (eprint:  
 557 <https://onlinelibrary.wiley.com/doi/pdf/10.2307/2347485>) doi: 10.2307/  
 558 2347485
- 559 Hausfather, Z., & Peters, G. P. (2020, November). RCP8.5 is a problematic scenario  
 560 for near-term emissions. *Proceedings of the National Academy of Sciences*,  
 561 117(45), 27791–27792. Retrieved 2024-02-20, from [https://www.pnas.org/](https://www.pnas.org/doi/10.1073/pnas.2017124117)  
 562 [doi/10.1073/pnas.2017124117](https://www.pnas.org/doi/10.1073/pnas.2017124117) (Publisher: Proceedings of the National  
 563 Academy of Sciences) doi: 10.1073/pnas.2017124117
- 564 Henry, M., Merlis, T. M., Lutsko, N. J., & Rose, B. E. J. (2021, March). De-  
 565 composing the Drivers of Polar Amplification with a Single-Column Model.  
 566 *Journal of Climate*, 34(6), 2355–2365. Retrieved 2023-05-05, from [https://](https://journals.ametsoc.org/view/journals/clim/34/6/JCLI-D-20-0178.1.xml)  
 567 [journals.ametsoc.org/view/journals/clim/34/6/JCLI-D-20-0178.1.xml](https://journals.ametsoc.org/view/journals/clim/34/6/JCLI-D-20-0178.1.xml)  
 568 (Publisher: American Meteorological Society Section: Journal of Climate) doi:  
 569 10.1175/JCLI-D-20-0178.1
- 570 Kahl, J. D. W., Zaitseva, N. A., Khattatov, V., Schnell, R. C., Bacon, D. M., Ba-  
 571 con, J., ... Serreze, M. C. (1999). Radiosonde Observations from the Former  
 572 Soviet “North Pole” Series of Drifting Ice Stations, 1954–90. *Bulletin of the*  
 573 *American Meteorological Society*, 80(10), 2019–2026. Retrieved 2023-04-20,  
 574 from <https://www.jstor.org/stable/26214953> (Publisher: American  
 575 Meteorological Society)
- 576 Krumpen, T., von Albedyll, L., Goessling, H. F., Hendricks, S., Juhls, B., Spreen,  
 577 G., ... Sokolova, J. (2021, August). MOSAiC drift expedition from Octo-  
 578 ber 2019 to July 2020: sea ice conditions from space and comparison with  
 579 previous years. *The Cryosphere*, 15(8), 3897–3920. Retrieved 2024-02-09,  
 580 from <https://tc.copernicus.org/articles/15/3897/2021/> (Publisher:  
 581 Copernicus GmbH) doi: 10.5194/tc-15-3897-2021
- 582 Liu, Y., Key, J. R., Schweiger, A., & Francis, J. (2006, October). Characteristics  
 583 of Satellite-Derived Clear-Sky Atmospheric Temperature Inversion Strength  
 584 in the Arctic, 1980–96. *Journal of Climate*, 19(19), 4902–4913. Retrieved  
 585 2024-02-06, from [https://journals.ametsoc.org/view/journals/clim/19/](https://journals.ametsoc.org/view/journals/clim/19/19/jcli3915.1.xml)  
 586 [19/jcli3915.1.xml](https://journals.ametsoc.org/view/journals/clim/19/19/jcli3915.1.xml) (Publisher: American Meteorological Society Section:  
 587 Journal of Climate) doi: 10.1175/JCLI3915.1
- 588 Lu, J., & Cai, M. (2010, April). Quantifying contributions to polar warming am-  
 589 plification in an idealized coupled general circulation model. *Climate Dynam-*  
 590 *ics*, 34(5), 669–687. Retrieved 2023-09-25, from [https://doi.org/10.1007/](https://doi.org/10.1007/s00382-009-0673-x)  
 591 [s00382-009-0673-x](https://doi.org/10.1007/s00382-009-0673-x) doi: 10.1007/s00382-009-0673-x
- 592 Manabe, S., & Wetherald, R. T. (1975, January). The Effects of Doubling  
 593 the CO<sub>2</sub> Concentration on the climate of a General Circulation Model.  
 594 *Journal of the Atmospheric Sciences*, 32(1), 3–15. Retrieved 2023-09-  
 595 25, from [https://journals.ametsoc.org/view/journals/atasc/32/1/](https://journals.ametsoc.org/view/journals/atasc/32/1/1520-0469.1975.032.0003.teodtc.2.0.co.2.xml)  
 596 [1520-0469.1975.032.0003.teodtc.2.0.co.2.xml](https://journals.ametsoc.org/view/journals/atasc/32/1/1520-0469.1975.032.0003.teodtc.2.0.co.2.xml) (Publisher: American  
 597 Meteorological Society Section: Journal of the Atmospheric Sciences) doi:  
 598 10.1175/1520-0469(1975)032<0003:TEODTC>2.0.CO;2
- 599 Maturilli, M., Holdridge, D. J., Dahlke, S., Graeser, J., Sommerfeld, A., Jaiser,  
 600 R., ... Schulz, A. (2021). *Initial radiosonde data from 2019-10 to 2020-*  
 601 *09 during project MOSAiC*. PANGAEA. Retrieved 2024-02-06, from  
 602 <https://doi.pangaea.de/10.1594/PANGAEA.928656> (Publication Title:  
 603 Alfred Wegener Institute, Helmholtz Centre for Polar and Marine Research,

- Bremerhaven) doi: 10.1594/PANGAEA.928656
- Medeiros, B., Deser, C., Tomas, R. A., & Kay, J. E. (2011, September). Arctic Inversion Strength in Climate Models. *Journal of Climate*, 24(17), 4733–4740. Retrieved 2023-10-24, from <https://journals.ametsoc.org/view/journals/clim/24/17/2011jcli3968.1.xml> (Publisher: American Meteorological Society Section: Journal of Climate) doi: 10.1175/2011JCLI3968.1
- Notz, D., & Community, S. (2020). Arctic Sea Ice in CMIP6. *Geophysical Research Letters*, 47(10), e2019GL086749. Retrieved 2022-12-31, from <https://onlinelibrary.wiley.com/doi/abs/10.1029/2019GL086749> (\_eprint: <https://onlinelibrary.wiley.com/doi/pdf/10.1029/2019GL086749>) doi: 10.1029/2019GL086749
- Otosaka, I. N., Shepherd, A., Ivins, E. R., Schlegel, N.-J., Amory, C., van den Broeke, M. R., ... Wouters, B. (2023, April). Mass balance of the Greenland and Antarctic ice sheets from 1992 to 2020. *Earth System Science Data*, 15(4), 1597–1616. Retrieved 2024-02-05, from <https://essd.copernicus.org/articles/15/1597/2023/> (Publisher: Copernicus GmbH) doi: 10.5194/essd-15-1597-2023
- Pattyn, F., Ritz, C., Hanna, E., Asay-Davis, X., DeConto, R., Durand, G., ... van den Broeke, M. (2018, December). The Greenland and Antarctic ice sheets under 1.5 °C global warming. *Nature Climate Change*, 8(12), 1053–1061. Retrieved 2023-05-08, from <https://www.nature.com/articles/s41558-018-0305-8> (Number: 12 Publisher: Nature Publishing Group) doi: 10.1038/s41558-018-0305-8
- Peng, S., Yang, Q., Shupe, M. D., Xi, X., Han, B., Chen, D., ... Liu, C. (2023, August). The characteristics of atmospheric boundary layer height over the Arctic Ocean during MOSAiC. *Atmospheric Chemistry and Physics*, 23(15), 8683–8703. Retrieved 2024-01-16, from <https://acp.copernicus.org/articles/23/8683/2023/> (Publisher: Copernicus GmbH) doi: 10.5194/acp-23-8683-2023
- Perovich, D. K., Grenfell, T. C., Richter-Menge, J. A., Light, B., Tucker III, W. B., & Eicken, H. (2003). Thin and thinner: Sea ice mass balance measurements during SHEBA. *Journal of Geophysical Research: Oceans*, 108(C3). Retrieved 2024-02-09, from <https://onlinelibrary.wiley.com/doi/abs/10.1029/2001JC001079> (\_eprint: <https://onlinelibrary.wiley.com/doi/pdf/10.1029/2001JC001079>) doi: 10.1029/2001JC001079
- Persson, P. O. G., Fairall, C. W., Andreas, E. L., Guest, P. S., & Perovich, D. K. (2002). Measurements near the Atmospheric Surface Flux Group tower at SHEBA: Near-surface conditions and surface energy budget. *Journal of Geophysical Research: Oceans*, 107(C10), SHE 21–1–SHE 21–35. Retrieved 2024-02-06, from <https://onlinelibrary.wiley.com/doi/abs/10.1029/2000JC000705> (\_eprint: <https://onlinelibrary.wiley.com/doi/pdf/10.1029/2000JC000705>) doi: 10.1029/2000JC000705
- Pistone, K., Eisenman, I., & Ramanathan, V. (2014, March). Observational determination of albedo decrease caused by vanishing Arctic sea ice. *Proceedings of the National Academy of Sciences*, 111(9), 3322–3326. Retrieved 2022-03-06, from <https://pnas.org/doi/full/10.1073/pnas.1318201111> doi: 10.1073/pnas.1318201111
- Pithan, F., & Mauritsen, T. (2014, March). Arctic amplification dominated by temperature feedbacks in contemporary climate models. *Nature Geoscience*, 7(3), 181–184. Retrieved 2022-02-14, from <https://www.nature.com/articles/ngeo2071> (Number: 3 Publisher: Nature Publishing Group) doi: 10.1038/ngeo2071
- Pithan, F., Medeiros, B., & Mauritsen, T. (2014, July). Mixed-phase clouds cause



- climate model biases in Arctic wintertime temperature inversions. *Climate Dynamics*, 43(1), 289–303. Retrieved 2023-06-17, from <https://doi.org/10.1007/s00382-013-1964-9> doi: 10.1007/s00382-013-1964-9
- Rantanen, M., Karpechko, A. Y., Lipponen, A., Nordling, K., Hyvärinen, O., Ruosteenoja, K., ... Laaksonen, A. (2022, August). The Arctic has warmed nearly four times faster than the globe since 1979. *Communications Earth & Environment*, 3(1), 1–10. Retrieved 2022-08-11, from <https://www.nature.com/articles/s43247-022-00498-3> (Number: 1 Publisher: Nature Publishing Group) doi: 10.1038/s43247-022-00498-3
- Reynolds, R., & Riihimäki, L. (2019, October). ARM: ICERAD. doi: 10.5439/1608608
- Saavedra Garfias, P., Kalesse-Los, H., von Albedyll, L., Griesche, H., & Spreen, G. (2023, November). Asymmetries in cloud microphysical properties ascribed to sea ice leads via water vapour transport in the central Arctic. *Atmospheric Chemistry and Physics*, 23(22), 14521–14546. Retrieved 2024-02-05, from <https://acp.copernicus.org/articles/23/14521/2023/> (Publisher: Copernicus GmbH) doi: 10.5194/acp-23-14521-2023
- Shupe, M. D., Rex, M., Blomquist, B., Persson, P. O. G., Schmale, J., Uttal, T., ... Yue, F. (2022, February). Overview of the MOSAiC expedition: Atmosphere. *Elementa: Science of the Anthropocene*, 10(1), 00060. Retrieved 2023-03-27, from <https://doi.org/10.1525/elementa.2021.00060> doi: 10.1525/elementa.2021.00060
- Solomon, A., Shupe, M. D., Svensson, G., Barton, N. P., Batrak, Y., Bazile, E., ... Tolstykh, M. (2023, April). The winter central Arctic surface energy budget: A model evaluation using observations from the MOSAiC campaign. *Elementa: Science of the Anthropocene*, 11(1), 00104. Retrieved 2023-06-07, from <https://doi.org/10.1525/elementa.2022.00104> doi: 10.1525/elementa.2022.00104
- Stramler, K., Genio, A. D. D., & Rossow, W. B. (2011, March). Synoptically Driven Arctic Winter States. *Journal of Climate*, 24(6), 1747–1762. Retrieved 2023-06-17, from <https://journals.ametsoc.org/view/journals/clim/24/6/2010jcli3817.1.xml> (Publisher: American Meteorological Society Section: Journal of Climate) doi: 10.1175/2010JCLI3817.1
- Taylor, P. C., Boeke, R. C., Boisvert, L. N., Feldl, N., Henry, M., Huang, Y., ... Tan, I. (2022). Process Drivers, Inter-Model Spread, and the Path Forward: A Review of Amplified Arctic Warming. *Frontiers in Earth Science*, 9. Retrieved 2022-02-10, from <https://www.frontiersin.org/article/10.3389/feart.2021.758361>
- The IMBIE Team. (2020, March). Mass balance of the Greenland Ice Sheet from 1992 to 2018. *Nature*, 579(7798), 233–239. Retrieved 2023-05-06, from <https://www.nature.com/articles/s41586-019-1855-2> (Number: 7798 Publisher: Nature Publishing Group) doi: 10.1038/s41586-019-1855-2
- Uttal, T., Curry, J. A., McPhee, M. G., Perovich, D. K., Moritz, R. E., Maslanik, J. A., ... Grenfeld, T. C. (2002, February). Surface Heat Budget of the Arctic Ocean. *Bulletin of the American Meteorological Society*, 83(2), 255–276. Retrieved 2023-04-12, from [https://journals.ametsoc.org/view/journals/bams/83/2/1520-0477\\_2002\\_083\\_0255\\_shbota\\_2\\_3\\_co\\_2.xml](https://journals.ametsoc.org/view/journals/bams/83/2/1520-0477_2002_083_0255_shbota_2_3_co_2.xml) (Publisher: American Meteorological Society Section: Bulletin of the American Meteorological Society) doi: 10.1175/1520-0477(2002)083<0255:SHBOTA>2.3.CO;2
- Walsh, W. L. C. F. F., J. E., & Stewart, J. S. (2019). *Gridded Monthly Sea Ice Extent and Concentration, 1850 Onward, Version 2*. National Snow and Ice Data Center. Retrieved from <https://nsidc.org/data/G10010/versions/2> doi: 10.7265/jj4s-tq79
- Wexler, H. (1936, April). COOLING IN THE LOWER ATMOSPHERE AND THE STRUCTURE OF POLAR CONTINENTAL AIR. *Monthly Weather Review*,



64(4), 122–136. Retrieved 2024-02-05, from [https://journals.ametsoc.org/view/journals/mwre/64/4/1520-0493.1936.64\\_122\\_citlaa\\_2.0\\_co.2.xml](https://journals.ametsoc.org/view/journals/mwre/64/4/1520-0493.1936.64_122_citlaa_2.0_co.2.xml)  
(Publisher: American Meteorological Society Section: Monthly Weather Review) doi: 10.1175/1520-0493(1936)64(122:CITLAA)2.0.CO;2  
Wiel, B. J. H. V. d., Vignon, E., Baas, P., Hooijdonk, I. G. S. v., Linden, S. J. A. v. d., Hooft, J. A. v., ... Genthon, C. (2017, April). Regime Transitions in Near-Surface Temperature Inversions: A Conceptual Model. *Journal of the Atmospheric Sciences*, 74(4), 1057–1073. Retrieved 2023-10-24, from <https://journals.ametsoc.org/view/journals/atsc/74/4/jas-d-16-0180.1.xml> (Publisher: American Meteorological Society Section: Journal of the Atmospheric Sciences) doi: 10.1175/JAS-D-16-0180.1  
Woods, C., & Caballero, R. (2016, June). The Role of Moist Intrusions in Winter Arctic Warming and Sea Ice Decline. *Journal of Climate*, 29(12), 4473–4485. Retrieved 2024-02-05, from <https://journals.ametsoc.org/view/journals/clim/29/12/jcli-d-15-0773.1.xml> (Publisher: American Meteorological Society Section: Journal of Climate) doi: 10.1175/JCLI-D-15-0773.1